Tailoring the Surface Properties of ZnO Nanowires by ALD Deposition

Camilla Baratto, Guido Faglia, Thi Than Le Dang, Matteo Ferroni, Viktoria Holovanova, Bohdan Nazarchuk, Hanna Hakola, Tapio Niemi, Nikolai Tkachenko, and Viacheslav Golovanov*

Innovative research on metal-oxide gas sensors involves nanostructuring and surface modification as key elements to tailor sensitivity and selectivity. This work addresses a ZnO nanowire-based sensing device obtained by coupling a lithographically prepared substrate with hydrothermal ZnO growth, to align and interconnect the nanowires between two electrical contacts. Furthermore, conformal coating by atomic layer deposition technique allows functionalization of the surface of the nanowires with sub-monolayers of Al_2O_3 and TiO_2. A detailed analysis is carried out from a morphological and structural point of view with photoluminescence and Raman spectroscopy and electron microscopy. The material characterization results are analyzed in comparison with the functional characterization in gases toward reducing (NO_2) and oxidizing (H_2S) gases. Unparalleled sensing enhancement with Atomic Layer Deposition functionalization is obtained for NO_2 detection. The passivation role of surface states is discussed combining information from experimental techniques with a proposed model.

1. Introduction

Nanostructures of semiconductor oxides play a crucial role in the field of gas sensors due to their unique properties and high volume to surface ratio.[1–3] These nanostructures provide a large surface area for gas molecules to interact with, leading to enhanced gas sensing capabilities. To realize reliable gas sensing devices that can be scaled up for industrial applications, it is important to consider the fabrication process of nanostructures. Most nanostructures are fabricated using bottom-up techniques such as vapor–liquid–solid (VLS) deposition,[4,5] hydrothermal growth,[6] and chemical vapor deposition (CVD).[7] These techniques often require post-fabrication strategies, including the transfer of nanowires (NWs) to a different substrate and the formation of appropriate electrical contacts using expensive techniques like nanolithography.[2] Therefore, it is crucial to explore bottom-up deposition techniques that enable the alignment and interconnection of nanostructures between two contacts. Our previous work investigated several individual NWs aligned between contacts by Langmuir Blodgett technique, but the conductance of the realized device was too low for practical use.[8] An interesting approach to obtain nearly horizontal nanowires on a specially designed chip is obtained by selective

---

C. Baratto, G. Faglia
CNR-INO Unit of Brescia and DII
University of Brescia
Via Branze 45, Brescia 25123, Italy
E-mail: camilla.baratto@ino.cnr.it

T. T. L. Dang
Faculty of Electronic Materials and Devices
School of Materials Science and Engineering (SMSE)
Hanoi
University of Science and Technology (HUST)
No. 1, Dai Co Viet Str., Hanoi 100000, Vietnam

The ORCID identification number(s) for the author(s) of this article can be found under https://doi.org/10.1002/admt.202400937

[†] Deceased

DOI: 10.1002/admt.202400937

M. Ferroni
DICATAM
University of Brescia
Via Branze 45, Brescia 25123, Italy

M. Ferroni
CNR-IMM
Via Gobetti, 101, Bologna 40129, Italy

V. Holovanova, B. Nazarchuk, V. Golovanov
South–Ukrainian National University
Staroportofrankovskaya str. 26, Odessa 65020, Ukraine

H. Hakola, T. Niemi, N. Tkachenko†, V. Golovanov
Faculty of Engineering and Natural Sciences
Tampere University
Korkeakoulunkatu, Tampere FIN-33720, Finland

hydrothermal growth.[9,10] Our study utilizes a similar methodology to create inter-crossed NWs with appropriate conductance, thereby enabling the production of gas sensing devices to scale up.

A limitation of metal oxide gas sensors is their lack of selectivity. To address this issue, researchers have explored various approaches, including surface decoration with noble metals,[11–13] or other metal oxides that act as catalysts for specific gases of interest. In addition, heterojunctions between p-type,[14,15] or n-type oxides[16,17] have been investigated to enhance sensor selectivity. Techniques to reduce lattice mismatch between core-shell heterostructures can also be applied.[18] By utilizing sensors with slightly different olfactory patterns based on similar nanostructured oxides, electronic noses can be developed.[19]

The atomic layer deposition (ALD) technique is a chemical gas phase deposition method that offers precise control over the thickness of ultra-thin oxide films, such as Al_2O_3 and TiO_2.[20–22] This technique allows for a conformal coating on 3D nanostructured materials, including semiconductor oxides. In the contest of gas sensing, ALD conformal depositions of ZnO with thickness in the range from 10 to 50 nm was employed to improve sensing performance of nanorods,[23] or to create a thick film that acts as a filter, or as nanomembranes.[24,25] Nevertheless, thinner ALD deposition of metal oxides over NWs were not investigated in literature. The aim of this work is to achieve a sub-monolayer coating that slightly modifies the surface of ZnO[26] without blocking the active sites responsible for gas detection. This approach stems out from the observation that the initial cycles of ALD can passivate surface traps in metal oxide semiconductors employed in water splitting.[22] Based on their well-known catalytic activity,[27,28] Al_2O_3 and TiO_2 were selected as ALD layers for the modification of the ZnO surface. Our research included both Al and Ti due to their diverse valence states and radii: we were interested in learning more about their effect on sensing characteristics.

To our knowledge, there is no research on the effect of low-thickness ALD modification of ZnO for sensing.

Since mid-twentieth century, the accepted working principle of semiconductor gas sensors has been dominated by the so-called "ionosorption" model[29]: target species reacted with surface ionosorbed oxygen species affecting conductivity by modulating the height of surface to bulk voltage, while lattice oxygen vacancies were deemed frozen and simply acting as donors.

At the beginning of the 21st century, prompted by the lack of spectroscopical evidence of ionosorbed oxygen, a few seminal works by Barsan and Gurlo[30–33] have questioned the model and demonstrated the role of surface oxygen vacancies in semiconductor gas sensors. Meanwhile experiments and theory have shown that -at least in ZnO samples – O vacancies are deep donors, while Zn interstitials are too mobile to be stable at room temperature. Group-III (among which Al and Ti) and H impurities account for most of the n-type conductivity.[34,35] The possible role of surface and bulk oxygen vacancies in sensing has therefore become an important topic of discussion and study.[36–39]

In this manuscript, we present a comprehensive investigation of the sensing properties of ZnO nanowires (NWs) and ZnO NWs modified with sub-monolayer-thick Al_2O_3 and TiO_2, with a discussion on the possible passivation role of ALD on surface states. Our study not only focuses on the gas sensing performance of these nanostructures but also includes a detailed analysis of their morphological and structural characteristics using PL/Raman and SEM/TEM techniques. By correlating the sensing properties with the responses to paradigm oxidizing and reducing gases such as NO_2 and H_2S, we aim to gain a deeper understanding of the relationship between the nanostructure design, surface modification, and gas sensing performance.

2. Experimental Section

2.1. Fabrication of Sensor Device Structure and Growth of ZnO NWs

To reliably connect nearby contact with bridging NWs, the procedure used to grow horizontal NWs was readapted,[9] by designing and realizing a sensor platform with engineered distance between electrodes: the distance should be small enough to allow NWs grown from each side of the contact to connect between each other creating a bridge structure (**Figure 1**).

2.1.1. Sensor Platform

To confine the growth of ZnO NWs to in-plane region, a guiding structure was fabricated by photolithography. This structure acted both as an electrode and a template for the growth of the NWs. The electrode's configuration is shown in Figure 1a.

The structure shown in Figure 1a was fabricated by photolithography using a commercial image-reversal photoresist AZ-5214E from MicroChemicals. A wafer with 100 nm layer of Si_3N_4 on Si/SiO_2 was used as a substrate.

2.1.2. ZnO Layer

The samples were sputtered with ZnO using a sputter coater (Edwards S150) with a Zinc target (Matsurf Technologies Inc, 99.99%). A vacuum of $2{\cdot}10^{-1}$ torr and 30 mA sputtering current were used to conduct all experiments. The thickness of the ZnO layer was set to 50 nm.

2.1.3. Au Electrodes and Lift-Off

A 10 nm film of titanium was deposited on top of the zinc layer to act as an adhesion between zinc and a gold layer of 150 nm. The evaporation of the metal was performed using electron-beam evaporator with an evaporation rate of 0.05 and 0.15 nm s^{-1} for titanium and gold respectively. Then, the substrate was placed inside an ultrasonic bath in acetone for 12 min and 2-propanol for 2 min. The electrode configuration depicted in Figure 1a was finally realized by this lift-off process.

2.1.4. Bridged ZnO Nanowires

As a last step, ZnO NWs were synthesized following the procedure reported earlier.[40] The microelectrode substrates were immersed with the active surface down into aqueous solution of

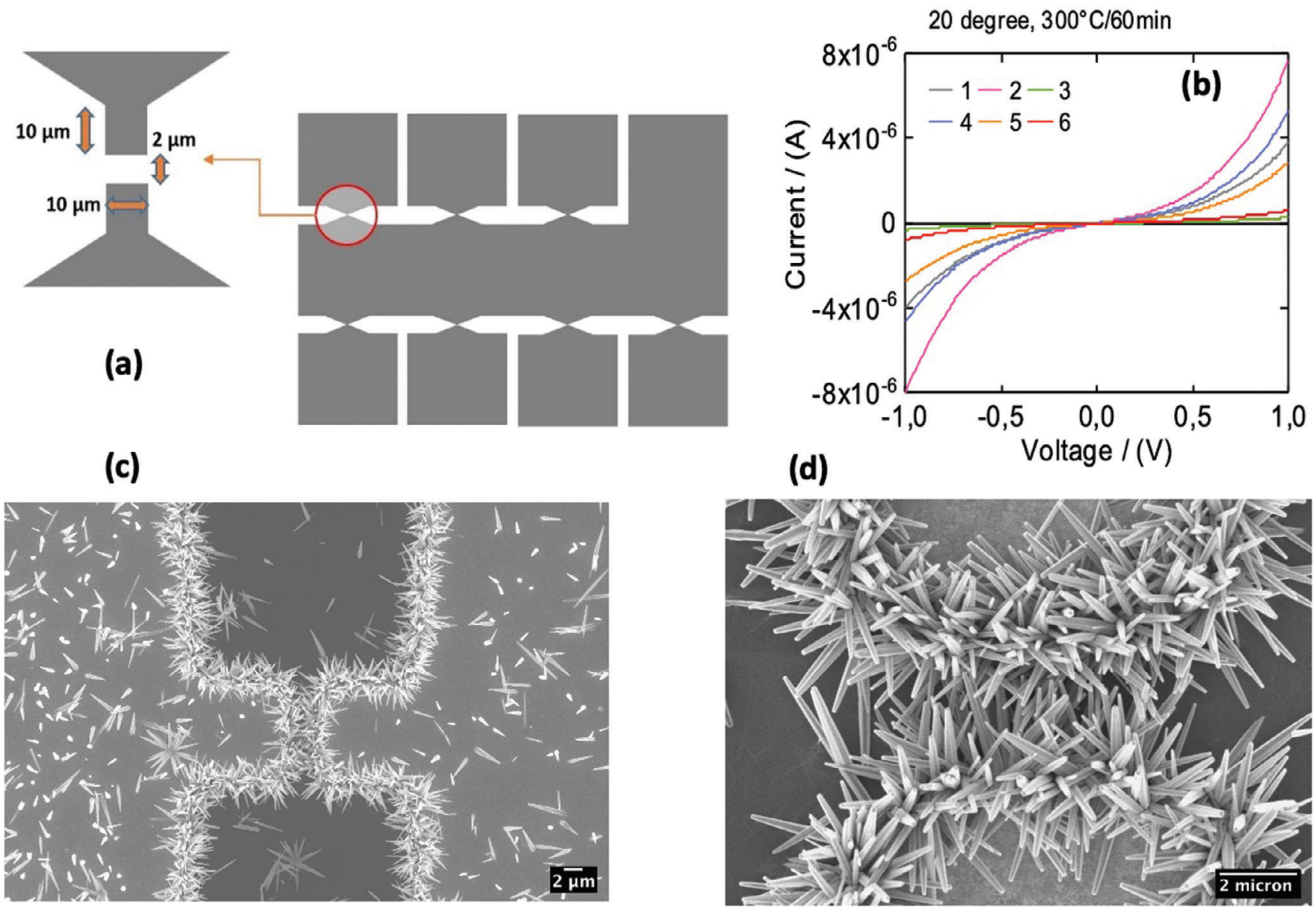

Figure 1. a) Set of seven electrodes with physical dimensions of each electrode pair; b) *I–V* characteristics of six pairs of electrodes with ZnO NWs; c) Low magnification SEM image of the device electrodes with NWs bridging the electrodes. The growth of NWs proceeds from the ZnO seed layer underneath the gold electrode. The NWs growth is selective. Very sporadic NWs growth can be observed in the area without contacts; d) SEM at higher magnification showing that only NWs contributing to conductions are the ones interconnecting between electrodes.

zinc nitrate (0.02 mol l^{-1}, ≥99%) and hexamethylenetetramine (0.02 mol/l, 99%) for 4 h. At the beginning, the solution was at room temperature and reached the target temperature (85 °C) in 1 h. After 3 h reaction at 85 °C, the samples were rinsed with Milli-Q water, and dried in air at room temperature. Finally, the samples were annealed in air (300 °C, 30 min).

Tapered NWs selectively grow from ZnO seed layer under electrodes and cross each other in between the electrodes, as shown in Figure 1c,d. IV curves acquired across different electrodes – Figure 1b – indicated a good conduction between electrodes for all of them, with a variability probably due to growth (number of crossing NWs per electrodes) which determines a different initial current.

2.2. Atomic Layer Deposition of TiO_2 and Al_2O_3 on ZnO NWs

The sensitivity and selectivity are determined by the surface reactions, and the surface passivation is expected to alter both selectivity and sensitivity. atomic layer deposition (ALD) is an affordable yet precise method to modify surface at the atomic scale. Another advantage of ALD is that the layers can be deposited on surfaces with complex topology, which is the case of nanowire structures shown in Figure 1d.

ALD deposition of sub-nanometer thick Al_2O_3 and TiO_2 films was carried out using a Picosun Sunale ALD R200 Advanced reactor. Trimethylaluminum (TMA) and deionized water were the Al and O sources in Al_2O_3 deposition. Tetrakis(dimethylamido)titanium(IV) ($Ti(N(CH_3)_2)_4$, TDMAT, 99%, Strem Chemicals Inc., France), and deionized water were the precursors for TiO_2 deposition. All the depositions were carried at 200 °C using N_2 (99.9999%, Oy AGA Ab, Finland) as a carrier/purge/venting gas, respectively. The growth rate for TiO_2 and Al_2O_3 were 0.0345 nm/cycle and 0.1 nm/cycle, respectively. Two ALD cycles were used to deposit Al_2O_3 and six to deposit TiO_2, which resulted in nominal layer thicknesses of 0.2 nm for both compounds. After deposition, the samples were annealed step at 300 °C in air for 30 min, to improve ohmic contacts in the structure.

It must be emphasized that with this low number of deposition's cycles, the grown layers are very different from bulk TiO_2 and Al_2O_3 materials, since the layer thickness is compatible or even smaller than the lattice period of the bulk material. Unfortunately, the formal stoichiometry of such extremely thin film cannot be determined, and one can expect a large variation in arrangements on the surface. However, the possibility could not completely rule out that the dopant metal atoms (Al, Ti) were either dispersed randomly across the surface or incorporated into the surface defects without forming new oxide phases.

2.3. Physicochemical Characterizations

Characterization of the nanosized material was carried out using different analytical and microscopy techniques.

2.3.1. Scanning and Transmission Microscopy

Zeiss Sigma Field Emission Scanning Electron Microscope (SEM) was used to study the morphology of the samples and local variations of emission of secondary electrons, related to sample conductivity. The low acceleration voltage of 1 kV for the SEM allowed collecting more information from the surface of ZnO NWs, such as local charging.

Thin sections of the sensing device for observation in the transmission electron microscope (TEM) were prepared by a Ga-ions Focused Ion Beam in a ZEISS Crossbeam 340 dual-beam FIB-SEM system. FIB lamellas were observed in a TECNAI F20 TEM, operated at 200 kV, and capable of compositional analysis at high spatial resolution with the Scanning-TEM imaging (STEM) mode combined with X-Ray Energy Dispersive Spectrometry (EDS).

2.3.2. Raman and PL Spectroscopy

The Raman spectra were excited with the 532 nm line of a solid-state laser. The scattered light was analyzed by means of a Horiba modular system equipped with single spectrometer and a Peltier cooled charge-coupled device (CCD) detector. Spectra were obtained using a confocal microscope with a long working-distance 50X objective.

The PL spectra were acquired by UV excitation at 325 nm with an He-Cd laser. The laser was focused on the sample with a 20xUV objective.

2.3.3. Sensing Tests

Sensing tests were carried out in a stainless-steel test chamber (1000 cm^3) with an integrated heater holder for the chip and a quartz glass that allows front lighting. A constant flux (300 $cm^3\ min^{-1}$) and 30% relative humidity (RH) were used for the measurements. Gas species (NO_2 and H_2S) are diluted in dry air and contained in certified bottles. A picoammeter (Keithley model 486) was used to measure the electrical current while applying a continuous bias to the sensor film. For sensing studies, a bias of 1 V was utilized. The chip with the devices does not have integrated heating, so an external hotplate was used to reach the working temperature, allowing heating from room temperature to 250 °C.

Relative response (RR) toward oxidizing gases was calculated as $(R_{gas}-R_{air})/R_{air}$, where R_{gas} is the steady state value of resistance in gas and R_{air} is the steady state value of resistance in air. Relative response toward reducing gases was calculated as $(I_{gas}-I_{air})/I_{air}$, where I_{gas} is the steady state value of current in gas and I_{gas} is the steady state value of current in air.

3. Results

3.1. SEM and TEM Characterization

Electron microscopy investigation provides the characteristics of the ZnO NWs and of the Ti-O functionalization. In **Figure 2**a,b two SEM images of a ZnO nanowire, functionalized with thin Ti_xO_y ALD layer, obtained with two different detectors for secondary electrons available in the SEM are compared. The first SEM image (obtained with In-Lens detector) highlights the details of the stepped lateral sides of the nanowire, which are responsible of the tapered shape for the nanowire; the second SEM image (obtained with conventional Everhart-Thorley detector) is more sensitive to the component of the secondary electron signal generated by beam electrons backscattered by the sample. In this case, more information is visible from the upper termination of the nanowire, which is non uniform in contrast. Section (c) of Figure 2 is a TEM image of the thin transverse section of a nanowire embedded in the FIB lamella: the cluster of low-contrast detail at the center of the section could be related to the SEM images and is ascribed to small porosity or crystal defectivity in the central part of the nanowire. These details are therefore extended along the NWs and not limited to the upper termination. Section (d) of Figure 2 magnifies the lateral sides of the nanowire, showing the sharp and straight termination for the section. No evidence of composition modulation from ZnO to TiO_2 external ALD layer is visible, however STEM and EDS spectroscopy was performed at the highest possible magnification and the presence of Ti ions at the NWs lateral side was detected (Figure 2f). Indeed, the sub-nanometric thickness expected for the TiO_2 ALD coverage resulted in a minimum amount of Ti, even though its detection was achieved. The electron diffraction pattern of the nanowire reported in Figure 2e) shows the systematic rows of diffracted beams organized in hexagonal symmetry, a clear indication of highly-ordered, single-crystalline arrangement for the ZnO nanowire.

The TEM observation of a lamella from a ZnO nanowire, functionalized with thin Al_2O_3 ALD layer provided similar results, confirming the crystalline ZnO habit and structure, while the detection of Al was at the limit of STEM ED capability.

3.2. Effect of ALD Layers on Sensors' Conductance

Although the presence of Ti or Al on the surface of NWs can be barely detected, the conductivity of the NWs changes gradually after just a few ALD cycles, as presented in **Figure 3**. The conductivity increases three–six times after ALD, though the thickness increase on ALD can be neglected as the average thickness of NWs is ≈200 nm and ALD increase it by 0.2 nm at maximum. This points to gradual decrease of the surface defects of ZnO NW and strong passivation effect of the ALD.

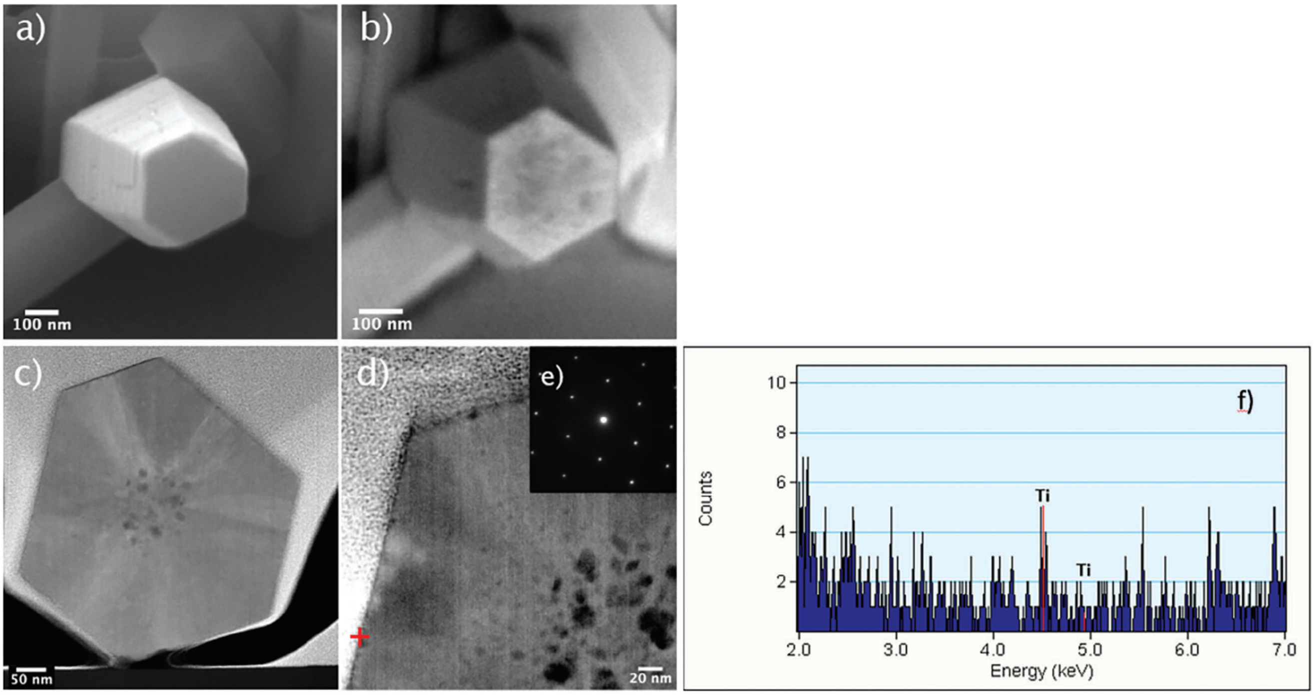

Figure 2. a) SEM image of the hexagonal shape of a TixOy functionalized ZnO nanowire and b) detail of the non-uniform morphology of the upper termination of the structure; c) TEM image of the FIB lamella featuring a thin section of the nanowire; d) detail of lateral termination of the nanowire, where no continuous layer of Ti oxide is observed at the surface of the ZnO nanowire; e) electron diffraction pattern from the ordered ZnO crystal structure of the nanowire. f) By focusing the e-beam at the NR surface (in the zone indicated by red cross), EDS spectroscopy confirms the detection of Ti at the NR surface.

3.3. Raman and PL Characterization

Raman scattering measurements allowed to obtain information about the sample quality and was here employed to confirm the crystalline phase of the ZnO NWs (**Figure** 4). Wurtzite type ZnO has several Raman active modes, and we observed the high-frequency E_2 mode at 438 cm^{-1} (E_2 $^{\text{high}}$), while the low-frequency E_2 mode was outside of the experimental range).[41] The broad peak above 1100 cm^{-1}, composed by a shoulder at 1105 cm^{-1} and a peak at 1148 cm^{-1} are assigned to second-order features reported by Cusco et al..[42]

One effective method for investigating the surface properties of ZnO NWs is the photoluminescence (PL) spectroscopy[43] In addition to the exciton-induced near-band-edge (NBE) photoluminescence, ZnO NWs exhibit visible emission as well. The visible emission band's spectral position is highly dependent on the preparation conditions and is ascribed to the existence of deep levels distributed in the band gap region: hence it is named deep level emission (DLE).[44] PL is a very sensitive "thermometer" of the surface states[45] which are involved in the sensing process; thus, we can study the PL spectra of the NWs to create a link to the sensing properties.

Figure 5 shows the PL emission of ZnO NWs and of ALD-modified ZnO. The raw PL spectrum is shown in – Figure 5a: we observe that ALD treatment produces a decrease in the PL

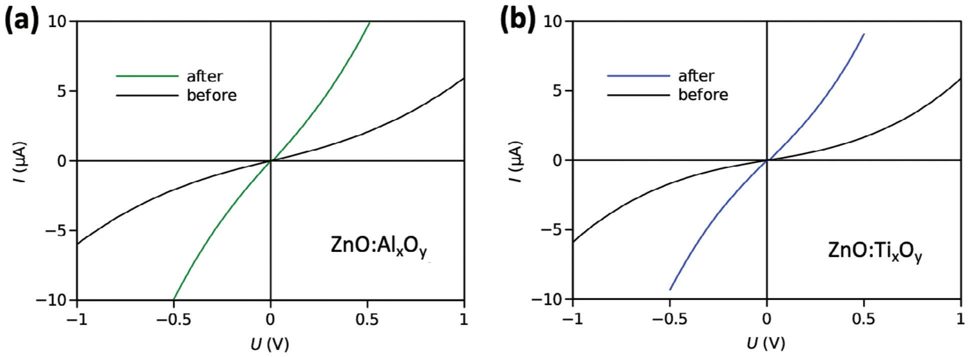

Figure 3. Current-voltage (*I–V*) characteristics of the nanowire samples recorded before and after ALD deposition of a) Al$_x$O$_y$ and b) Ti$_x$O$_y$ on ZnO NWs. An increase in the current after ALD deposition is observed.

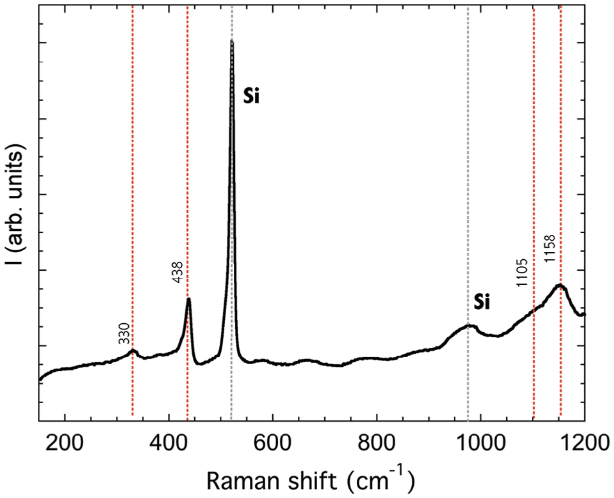

Figure 4. Visible Raman spectra up to 1200 cm^{-1} of ZnO NWs acquired with excitation line 532 nm, filter cut-off at 150 cm^{-1}; the reference positions of the modes are indicated with vertical dotted lines, red for ZnO and black for Si substrate.

emission on the whole spectrum. For the sake of comparison, the spectra were normalized to unit intensity: the spectrum – Figure 5b,c- shows NBE emission with a peak at 3.25 eV (381 nm) and green/yellow DLE emission. DLE peak was fitted by two Gaussian at 2.35 eV (528 nm) and 2.05 eV (605 nm).

Since the intensity is strongly dependent on the amount of NWs focused by the microscope objective, it is more appropriate to calculate the ratio A_{NBE}/A_{DLE}, where the A_{NBE} is area of the NBE peak (calculated between 350 and 450 nm) and A_{DLE} is the area of the DLE peaks (calculated between 540 and 660 nm). Studenikin et al.[43] reported that the higher the NBE emission is, the higher the quality of the ZnO NWs. Figure 5d reports $A_{NBE,}$ A_{DLE} and their ratio: in our case, the figure of merit A_{NBE}/A_{DLE} is used to evaluate if the ALD treatment produces a variation of defect states responsible for the visible emission (conventionally ascribed to oxygen vacancies[43,46,47]).

Both A_{NBE} and A_{DLE} decrease with the ALD treatment; their ratio increased for ZnO:Ti_xO_y deposition, while negligible increase was observed for ZnO:Al_xO_y.

The observed reduction of deep defect emission band is higher for ZnO:Ti_xO_y than for ZnO:$Al_xO_{y,}$ while an overall emission reduction is observed for both ALD treated samples (Figure 5a). DLE reduction was reported in literature for ZnO:ZnO homojunction for much higher number of cycles (50 cycles),[21] assigning it the oxygen vacancy reduction.

3.4. Sensing Properties

3.4.1. *Effect of Working Temperature on ZnO-based Sensors*

As a starting test, we investigated the effect of working temperature on the sensor's dynamic for the bare ZnO NWs sensors. **Figure 6** shows the sensor's dynamic from room temperature to 250 °C toward NO_2 and H_2S gases. Room temperature operation – Figure 6a – showed limited gas sensing performances to NO_2 along with incomplete recovery. To obtain a good NO_2 detection at room temperature, photoactivation could be used as an alternative source of energy activation instead of temperature.[8,48] When the temperature is raised to 200 °C response to NO_2 is interesting but the dynamic is still slow. For H_2S, relative response (*RR*) is small and incomplete recovery is observed – Figure 6b. At 250 °C NO_2 sensing is very good, and H_2S sensing is acceptable – Figure 6c. The observed spike in the 1 ppm measure is probably due to incorrect mixing dynamic between humid air and NO_2 at this concentration and temperature in our system, that is promptly indicated by sensors.

To quantify the observed dynamic variation of the current, we plotted the *RR* for NO_2 at 200 and 250 °C – Figure 6d. Very high *RR* of 64.3 was observed at 200 °C (7 ppm), if compared to lower 27.1 observed at 250 °C (7 ppm). Nevertheless, the compromise for a faster sensor indicates that 250 °C is the preferable working temperature.

For 250 °C working temperature we calculated the calibration curves by plotting R_{gas}/R_{air} for NO_2 and I_{gas}/I_{air} for H_2S as a function of the gas concentration _ Figure 6e,f. The calibration curves are fitted by a power law $y = Ax^B$. The parameters of the fit are [A = 3.3405, B = 1.0982, R = 0.99821] for NO_2 and [A = 1.3844, B = 0.47431, R = 0.99955].

We then extrapolated the detection limit at 250 °C for NO_2 (0.4 ppm) – Figure 6e – and for H_2S (1 ppm) – Figure 6f – by measuring the value at the intersection with the baseline resistance (current) in air normalized to 1, plus three times the baseline noise (the sensor baseline noise was ≈0.1 in all experiments).[49]

The time constants associated to response and recovery dynamics, fitted by exponential relaxation curves, are summarized in **Table 1**. Short response and recovery dynamics cannot be assessed in the current configuration due to the test chamber's physical limitations, which prevent a complete exchange of the chamber atmosphere from occurring in less than three min. A decrease in response and recovery time constants with the increase of the working temperature is observed, in agreement with other experimental results based on semiconducting oxide NWs sensors based on multiple NWs.[1] For NO_2 at 250 °C the response time constant is even lower than the test chamber's limitations. For H_2S an exception is observed, with shorter recovery time constant at the lower working temperature (200 °C): this is probably ascribable to the very limited current variation observed at 200 °C.

3.4.2. *Effect of Surface Functionalization*

We then considered how surface functionalization affects sensing properties of ZnO NWs at 250 °C. To investigate this, we performed sensing tests with NO_2 and H_2S on ALD modified devices and compared them with the bare ZnO one. **Figure 7** resume the results: section (a) reports dynamic current variation when NO_2 pulsed are introduced in humid air and section (b) reports *RR* calculated as a function of gas concentration. The experimental data are fitted by a power law $y = Ax^B$ (the parameters of the fit are reported in Table S1, Supporting Information).

Figure 7c,d is the bar plot of response and recovery times. The response time constant τ_{res} is decreased with ALD treatment from 120 to 40s and 35s respectively. Recovery time

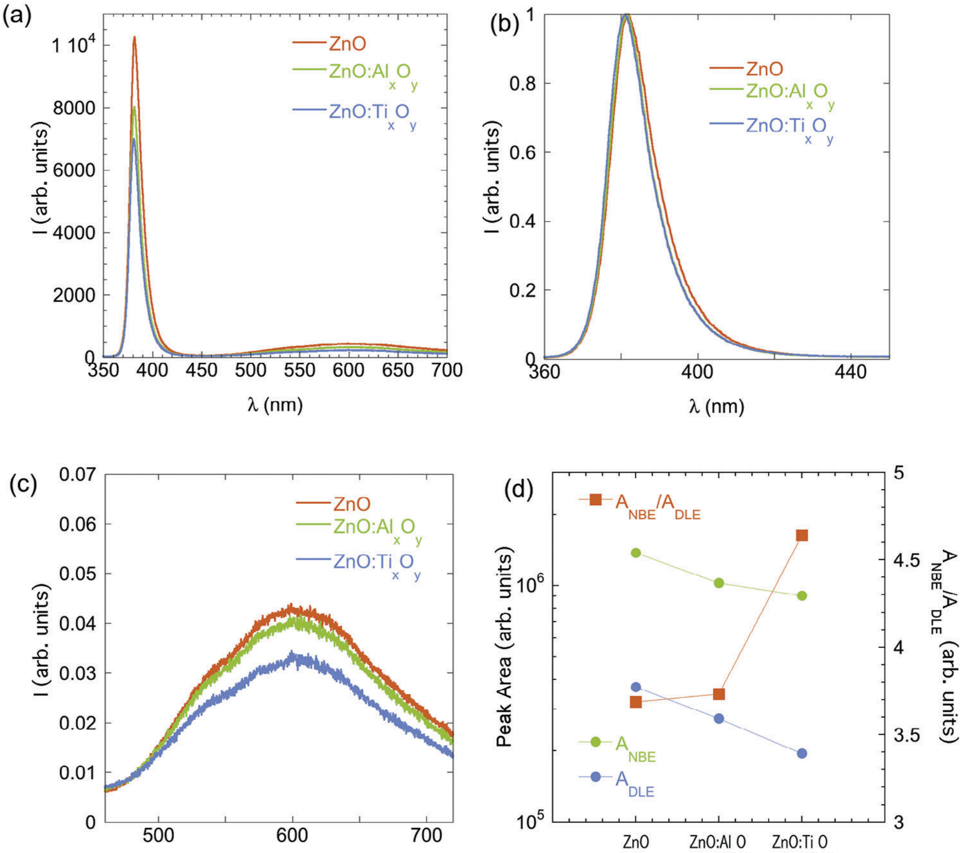

Figure 5. Normalized PL spectra acquired on ZnO, ZnO:Al$_x$O$_y$, ZnO:Ti$_x$O$_y$ a) Raw data, whole spectrum b) Normalized data, NBE emission; c) Normalized data, DLE emission; d) Comparison of integrated intensity of PL spectra over the samples.

constant τ_{rec} for ALD functionalized samples are slightly longer for ZnO:Al$_x$O$_y$ with respect to the ones measured for ZnO, probably due to higher *RR* observed in those cases. Notably τ_{rec} is smaller for ZnO:Ti$_x$O$_y$.

Bar plots of the *RR* for 7 ppm of NO$_2$ and of the *RR* for 7 ppm of H$_2$S are displayed in Figure 7e–f. Optimum results were obtained for ZnO:Al$_x$O$_y$, where the *RR* is increased from 26 to 68 for NO$_2$ detection, but an increase is also observed for ZnO:Ti$_x$O$_y$ (*RR* = 48). The increase is observable in H$_2$S detection as well, with *RR* raising from 1 to 2.3 for ZnO:Ti$_x$O$_y$ and to 2.8 for ZnO:Al$_x$O$_y$. We also notice that the *RR* for a reducing gas at 250 °C working temperature is one order of magnitude lower than the *RR* for an oxidizing gas in agreement with literature.[1] Higher working temperature tests will be the subject of further investigation in future work.

4. Discussion

Miniaturized devices based on ZnO cross-linked NWs proved effective in sensing reducing and oxidizing gases. Tailoring of the sensors' response is possible via conformal ALD deposition, even at low number of deposition cycles used in this work.

The formation of crystalline Al$_2$O$_3$ or TiO$_2$ -or their amorphous phases – is unlikely after a few ALD cycles. This conclusion is supported by TEM observations. Accordingly, we would not expect formation of heterostructure on the NW's surface.

The photoluminescence measurements (Figure 4) testify that ALD cures the surface defects in ZnO NWs. As these defects are acting as trapping centers of carriers, a decrease in defects population should result in an increase of the NWs conductivity upon the ALD treatment. This is exactly what was observed in IV curves, registered on the same sensor before and after the deposition (Figure 3). This conclusion agrees with results reported by Ghobadi et al. [22] where it was found that the first ALD cycle can significantly reduce the concentration of the surface traps. Based on the above, we can conclude that ALD treatment of ZnO surface, results in decrease of the surface barrier of the ZnO NWs. Eventually, the surface modification is beneficial both for H$_2$S and NO$_2$ sensing reactions (Figure 7), as it attracts more surface charge as compared with non-treated samples. This affects both the relative response (increased with respect to bare ZnO) and the response time (reduced to one-third of the bare ZnO device's values).

The different recovery times observed for NWs doped by Ti and Al could be due to different binding energies of NO$_2$ adsorbed on oxygen site of ZnO NW near the Al or Ti impurity.

As a benchmark, we compared the results obtained with literature research on conformal coating of ZnO by ALD deposited TiO$_2$ for gas sensing application: our work is the only

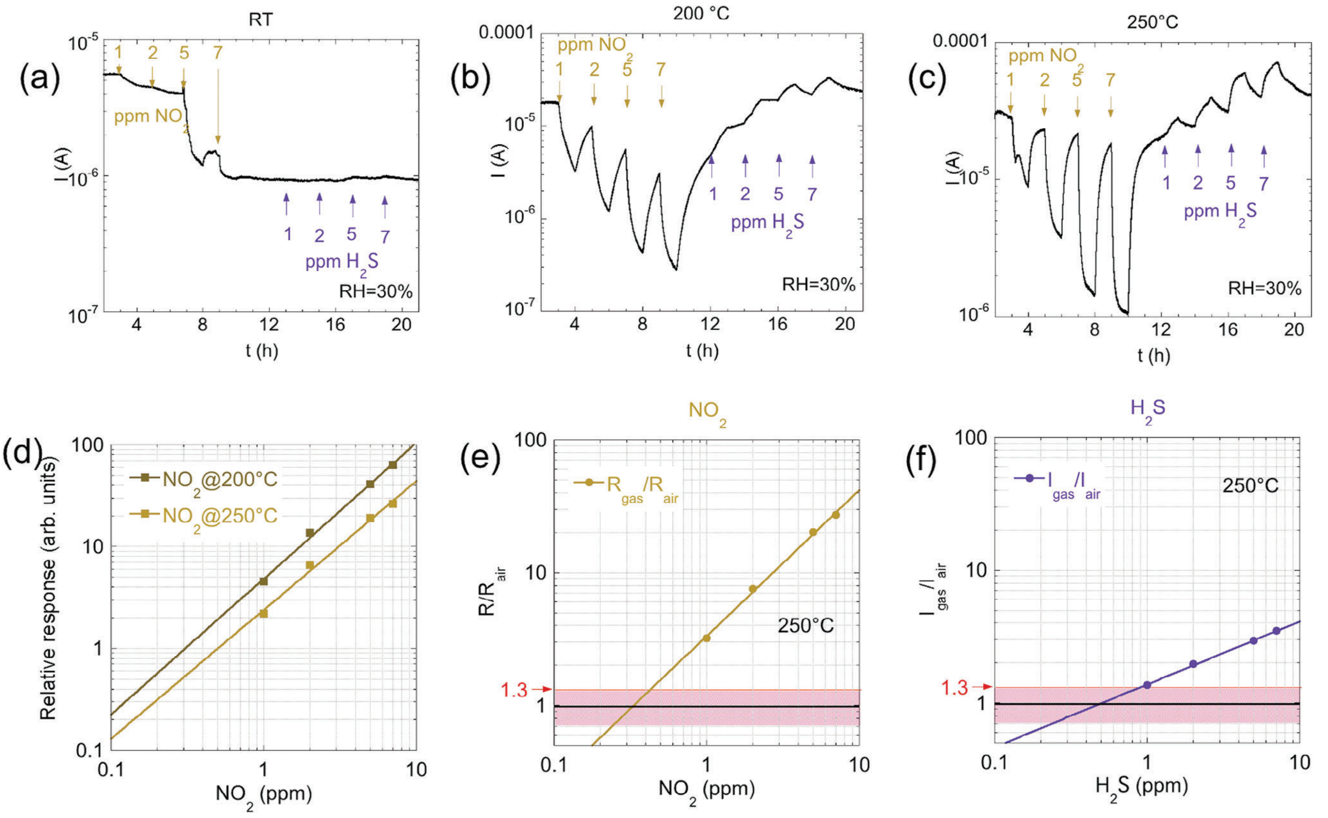

Figure 6. Top panel: Effect of the working temperature on the sensing properties of ZnO NWs device for NO2 and H2S: a) Room Temperature; b) 200 °C and c) 250 °C. d) Relative response RR = (R_{gas}-R_{air})/R_{air} at 200 and 250 °C for NO_2 detection. e) Detection limit for NO2 sensing at 250 °C, calculated by plotting the normalized resistance, and comparing it to the normalized resistance in air. f) Detection limit for H2S sensing at 250 °C, calculated by plotting the normalized current, and comparing it to the normalized current in air. The horizontal line at 1.3 depicted in red in the graphs (e,f) is the lower threshold for a discernible signal.

one to propose such reduced thicknesses of the Al_2O_3 coating layer for the functionalization of NWs. Thus, we considered heterostructures of ZnO/TiO_2 with higher thickness for comparison. Kwon at al.[50] reported an optimized relative response $RR = 4$ with 10 nm TiO_2 deposited by solution process on ZnO NWs. Extrapolating from the fit of our data, the RR at 10 ppm of our sensor would be $RR = 70$, significantly higher than the value in the literature; Ramgir et al.[51] reports a value of $R_{gas}/R_{air} = 7$, calculated for 5 ppm of NO_2, obtained by optimizing the TiO_2 deposition for ALD on ZnO NWs (30 nm thickness). In our work, calculating the R_{gas}/R_{air} value for our ZnO: Ti_xO_y sensor we obtain a value of 35, still higher than what is reported in the literature. For ZnO/ Al_2O_3 there is no direct comparison, as it was never used to enhance NO_2 detection.

Regarding the general sensing dynamic, the behavior of the base material, namely ZnO NWs should be considered. It is well-accepted that NWs exhibit better performance, when the Debye length is comparable to the diameter of NWs.[3,52] In other words, the smaller NW diameter, the better its sensitivity. We notice, however, that our structures based on the thick NWs demonstrate about one order of magnitude higher response to NO_2, than thinner NWs used in our previous study.[8] At the same time, the response and recovery times of these tapered NWs are remarkably slower. We concentrated here on explaining these unusual results because sensitivity and transient characteristics are among the key parameters for gas sensors,[53] which are essentially interrelated.

The non-ohmic IV characteristics presented in Figure 1b point out on buildup of back-to-back Schottky barriers, which can determine the functional parameters of our sensors. This may resemble the typical situation with the polycrystalline films, where modulation of the resistance at the grain boundaries stipulates the improved response of the sensor.[54] Furthermore, the presence of Schottky barriers may result in slower decay processes and persistent photoconductivity. This is exactly what we have observed in our experiments and is reported in Figures S1,S2 (Supporting Information).

Figure 8a,b reports the microscopic characterization of the area between gold contact and ZnO NW base area. To explore

Table 1. Time constants associated with response and recovery dynamics as a function of gaseous species and temperature (the constants were calculated at 7 ppm pulse).

	NO_2 200 °C	NO_2 250 °C	H_2S 200 °C	H_2S 250 °C
τ_{res} (s)	400	120	3200	1600
τ_{rec} (s)	2200	1900	2100	2800

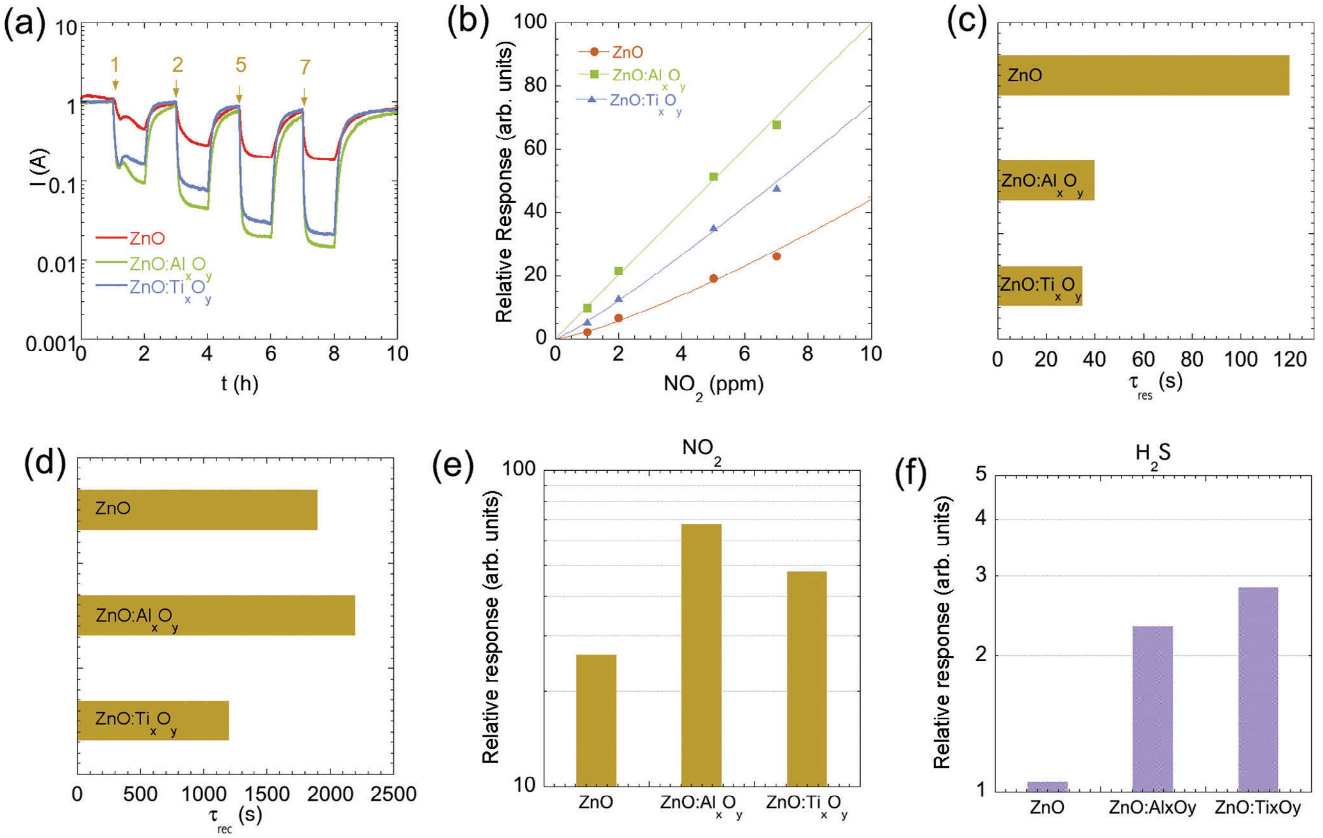

Figure 7. a) Dynamic response for NO_2 at 250 °C. b) Relative response – RR = $(R_{gas}-R_{air})/R_{air}$ – for ZnO and ALD functionalized NWs toward tested NO_2 concentrations (1,2,5,7 ppm) at 250 °C. The solid lines represent data fitting by power law; c) Bar plot of the response time constant (τ_{res}) for the sensors; d) Bar plot of recovery time constant (τ_{rec}) for the sensors; e) Bar plot of relative response versus NO_2 (7 ppm) (f). Bar plot that compares relative response $-(I_{gas}-I_{air})/I_{air}$ – versus H_2S (7 ppm) for the bare and functionalized NWs.

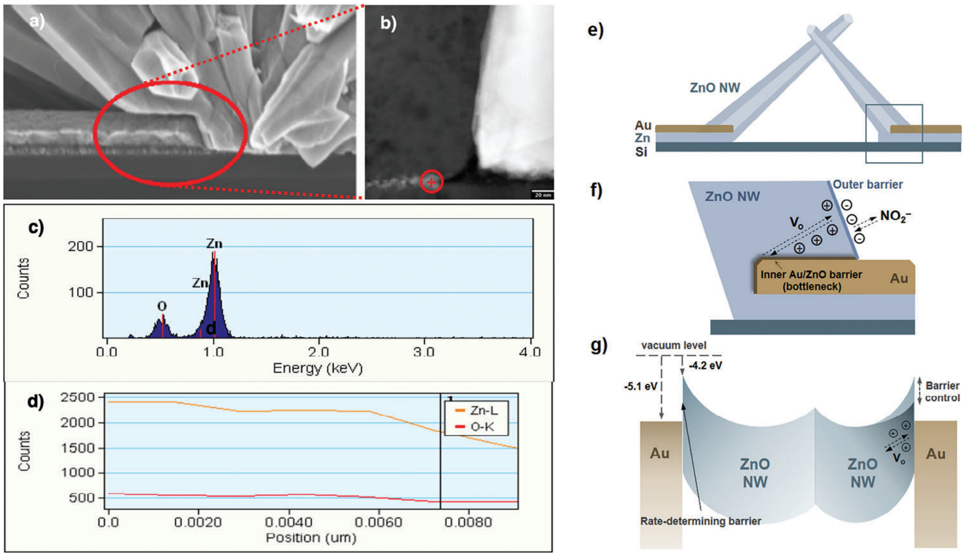

Figure 8. a) SEM image of the ZnO NWs grown from beneath of the gold electrode; b) STEM image of the inner ZnO/Au junction; c) energy – dispersive X-Ray spectrum collected at beam position marked by red mark; d) Zn/O peak integral variation across the interface; e) the schematic illustration of ZnO-nanowire bridges over the gold electrodes; f) energy band diagram of the bridged NWs, demonstrating Schottky barrier at the inner ZnO/Au interface.g) Oxygen vacancy redistribution at the junction between NWs and electrode.

the structure of NW/electrode interface, the precise STEM-EDS examination of our samples has been carried out. Figure 8a illustrates how the NWs are growing from beneath of the gold contacts, thus forming junctions that are not in contact with the gas phase. The detailed analysis of the Zn/O content at the interface revealed that the surface of the ZnO NWs is not subjected to disorder and no essential variation from stoichiometry has been detected (Figure 8c,d). The latter corroborates above-stated reasoning about formation of Schottky barrier at the ZnO/Au interface. In addition, STEM – EDS analysis at the junction showed that bright details marked by the red cross bar in the in Figure 8b, consist of a residual Au deposition originated during the lithographic process of contact fabrication.

The increased sensitivity of our inter-crossed NW structures can be associated with formation of the Schottky barriers either at NW/NW or at NW/electrode junctions (Figure 8e). In both cases, the sensor response is controlled by the potential barrier height rather than by the thickness of the conduction channel along the NW stem, narrowed by the surface electron depletion layer formed, e.g., by the adsorbed anionic NO_2 species. On the other hand, the unusually long response times observed in our structures, indicate that reactions are dominated by ionic processes, where diffusion of the defects through the lattice occurs to reach the equilibrium between the surface and the bulk of individual NW. This can happen, if the Schottky barriers are hidden between the electrodes and the inner side of the NWs – Figure 8f.

It is widely reported that presence of oxygen vacancies facilitates adsorption of acceptor-type molecules on metal oxides by attracting more surface charge compared with pristine material.[55,56] The adsorption of NO_2 at the ZnO nanowire sides opened to the gas phase breaks the surface electronic equilibrium and results in diffusion of oxygen vacancies to/from the bulk of the NW in response to the variation of its surface potential. Eventually, this affects redistribution of the oxygen vacancies nearby the NW/electrode junctions, which are the bottlenecks for adsorption reactions. Thus, the diffusion of oxygen vacancies is the rate-determining step, which limits response of our sensors – Figure 8g.

Numerous groups have reported issues in growing of ZnO single crystals on Au support. The Schottky barrier can be formed at the interface of ZnO/Au junction due to the larger work function of Au (5.1 eV)[57] as compared to the electron affinity of ZnO (4.2 eV).[58] It has been well documented however that gold can form both ohmic as well as Schottky junctions with n-type ZnO, depending on the presence of crystal defects on the surface of ZnO.[59–61]

5. Conclusion

In summary, comprehensive investigation of the sensing properties of ZnO NWs and ZnO NWs modified with Al_2O and TiO_2, enable to understand the effect of the surface modification role of an extremely thin layer deposited by ALD on the ZnO nanowire surface. The as grown samples exhibit single-crystalline arrangement for the ZnO NWs with hexagonal symmetry, as confirmed by TEM analysis. The NWs' diameters taper down to a minimum of roughly 300 nm at the end. Hence, rather than the thickness of the conduction channel along the NWs, the potential barrier height controls the sensor response, and the conductance from one nanowire to another is regulated either by inter-crossed NW junctions or at NW-electrode junctions.

No evidence of composition modulation from ZnO to TiO_2 or Al_2O_3 external ALD layer is visible through TEM investigation, however the presence of a minimum amount of Ti ions at the NWs lateral side was detected by EDX. For sample functionalized with thin Al_xO_y ALD layer the detection of Al was at the limit of STEM ED capability.

Nonetheless, ALD treatment is effective in increasing carriers available for conduction (enhanced current in IV) and in modifying PL spectra. The sensing properties of oxidizing and reducing model gases (NO_2 and H_2S) at the working temperature of 250 °C indicated that a higher relative response was obtained for Al_xO_y and Ti_xO_y, due to the decrease of the surface barrier in the ZnO NWs treated with ALD. The present study can promote the general understanding of the impact surface functionalization of ZnO NWs to improve their sensing ability.

Supporting Information

Supporting Information is available from the Wiley Online Library or from the author.

Acknowledgements

The authors of this paper express the sorrow for the untimely loss of Nikolai Tkachenko, a beautiful person and a valuable colleague. V.G. is grateful to the MSCA4Ukraine (No. 1233501), and the Academy of Finland (grant No. 353861) for financial support. This study was also funded by the European Union – Next Generation EU M4C2 1.1 within PRIN 2022 –2022JZAA9W.

Open access publishing facilitated by Consiglio Nazionale delle Ricerche, as part of the Wiley - CRUI-CARE agreement.

Conflict of Interest

The authors declare no conflict of interest.

Author Contributions

All authors had approved the final version of the manuscript. Conceptualization of the work (C.B., N.T, and V.G.); Nanowire synthesis: (H.H., V.H, and B.N.); device lithography (T.N.); SEM and TEM characterization (M.F.); Raman and photoluminescence characterization (C.B.); sensing tests (C.B. & T.T.L.D); data analysis and figures preparation (C.B., V.H., M.F., and G.F.); First draft writing (C.B.); funding acquisition (C.B., N.T., and V.G.).

Data Availability Statement

The data that support the findings of this study are available from the corresponding author upon reasonable request.

Keywords

atomic layer deposition (ALD), chemical sensors, nanowires, ZnO

Received: June 12, 2024
Revised: August 8, 2024

[1] C. Baratto, *RSC Adv.* **2018**, *8*, 32038.
[2] F. Hernández-Ramírez, A. Tarancón, O. Casals, J. Arbiol, A. Romano-Rodríguez, J. R. Morante, *Sens. Actuators, B* **2007**, *121*, 3.
[3] E. Comini, C. Baratto, G. Faglia, M. Ferroni, A. Vomiero, G. Sberveglieri, *Prog. Mater. Sci.* **2009**, *54*, 1.
[4] Z. L. Wang, *Mater. Sci. Eng. R Rep.* **2009**, *64*, 33.
[5] C. Baratto, S. Todros, G. Faglia, E. Comini, G. Sberveglieri, S. Lettieri, L. Santamaria, P. Maddalena, *Sens. Actuators, B* **2009**, *140*, 461.
[6] R. Milan, S. Cattarin, N. Comisso, C. Baratto, K. Kaunisto, N. V. Tkachenko, I. Concina, *Sci. Rep.* **2016**, *6*, 35049.
[7] X. Xing, K. Zheng, H. Xu, F. Fang, H. Shen, J. Zhang, J. Zhu, C. Ye, G. Cao, D. Sun, G. Chen, *Micron* **2006**, *37*, 370.
[8] C. Baratto, V. Golovanova, G. Faglia, H. Hakola, T. Niemi, N. Tkachenko, B. Nazarchurk, V. Golovanov, *Appl. Surf. Sci.* **2020**, *528*, 146959.
[9] Y. Qui, R. Yang, Z. L. Wang, *J. Phys. Chem. C* **2008**, *112*, 18734.
[10] W. J. Park, K. J. Choi, M. H. Kim, B. H. Koo, J. L. Lee, J. M. Baik, *ACS Appl. Mater. Interfaces* **2013**, *5*, 6802.
[11] O. Lupan, V. Cretu, V. Postica, M. Ahmadi, B. R. Cuenya, L. Chow, I. Tiginyanu, B. Viana, T. Pauporté, R. Adelung, *Sens. Actuators, B* **2016**, *223*, 893.
[12] P. Rai, Y. S. Kim, H. M. Song, M. K. Song, Y. T. Yu, *Sens. Actuators, B* **2012**, *165*, 133.
[13] J. Sun, X. Zhuang, Y. Fan, S. Guo, Z. Cheng, D. Liu, Y. Yin, Y. Tian, Z. Pang, Z. Wei, X. Song, L. Liao, F. Chen, J. C. Ho, Z. Yang, *Small* **2021**, *17*, 2102323.
[14] C. Baratto, R. Kumar, E. Comini, M. Ferroni, M. Campanini, *Nanotechnology* **2017**, *28*, 465502.
[15] Y. Liu, G. Li, R. Mi, C. Deng, P. Gao, *Sens. Actuators, B* **2014**, *191*, 537.
[16] Y. Xu, L. Zheng, C. Yang, W. Zheng, X. Liu, J. Zhang, *Sens. Actuators, B* **2020**, *310*, 127846.
[17] F. Liu, G. Huang, X. Wang, X. Xie, G. Xu, G. Lu, X. He, J. Tian, H. Cui, *Sens. Actuators, B* **2018**, *277*, 144.
[18] Z. Yang, N. Han, M. Fang, H. Lin, H. Cheung, S. Yip, E. Wang, T. Hung, C. Wong, J. C. Ho, *Nat. Commun.* **2014**, *5*, 1.
[19] A. Ponzoni, C. Baratto, N. Cattabiani, M. Falasconi, V. Galstyan, E. Nunez-Carmona, F. Rigoni, V. Sberveglieri, G. Zambotti, D. Zappa, *Sensors* **2017**, *17*, 714.
[20] G. Seguini, E. Cianci, C. Wiemer, D. Saynova, J. A. M. van Roosmalen, M. Perego, *Appl. Phys. Lett.* **2013**, *102*, 131603.
[21] I. S. Jeon, G. Bae, M. Jang, Y. Yoon, S. Jang, W. Song, S. Myung, J. Lim, S. S. Lee, H. K. Jung, J. Hwang, K. S. An, *Appl. Surf. Sci.* **2021**, *540*, 148350.
[22] A. Ghobadi, T. Gamze, U. Ghobadi, F. Karadas, *Sci. Rep.* **2018**, *8*, 16322
[23] A. Mirzaei, S. Park, H. Kheel, G. J. Sun, S. Lee, C. Lee, *Ceram. Int.* **2016**, *42*, 6187.
[24] M. Weber, O. Graniel, S. Balme, P. Miele, M. Bechelany, *Nanomaterials* **2019**, *9*, 1552.
[25] A. Rosental, A. Tarre, A. Gerst, A. Kasikov, J. Lu, M. Ottosson, T. Uustare, *IEEE Sens. J.* **2013**, *13*, 1648.
[26] C. Chen, H. He, Y. Lu, K. Wu, Z. Ye, *ACS Appl. Mater. Interfaces* **2013**, *5*, 6354.
[27] D. Langhammer, J. Kullgren, L. Österlund, *ACS Catal.* **2022**, *12*, 10472.
[28] E. Ozensoy, C. H. F. Peden, J. Szanyi, *J. Phys. Chem. B* **2005**, *109*, 15977.
[29] E. Comini, G. Faglia, G. Sberveglieri, in *Solid State Gas Sensing* (Eds.: E. Comini, G. Faglia, G. Sberveglieri), Springer US, Boston, MA, **2009**, pp. 1–61.
[30] A. Gurlo, ChemPhysChem, 2006,7,2041.
[31] I. Boehme, U. Weimar, N. Barsan, *Sens. Actuators, B* **2021**, *326*, 129004.
[32] D. Degler, S. Wicker, U. Weimar, N. Barsan, *J. Phys. Chem. C* **2015**, *119*, 11792.
[33] M. Hübner, C. E. Simion, A. Haensch, N. Barsan, U. Weimar, *Sens. Actuators, B* **2010**, *151*, 103.
[34] M. D. McCluskey, in *Defects in Advanced Electronic Materials and Novel Low Dimensional Structures* (Eds. J. Stehr, I. Buyanova, W. Chen), Woodhead Publishing, xx **2018**, pp. 1–25.
[35] M. Mccluskey, S. Jokela, *J. Appl. Phys.* **2009**, *106*, 71101.
[36] M. Epifani, J. D. Prades, E. Comini, E. Pellicer, M. Avella, P. Siciliano, G. Faglia, A. Cirera, R. Scotti, F. Morazzoni, J. R. Morante, *J. Phys. Chem. C* **2008**, *112*, 19540.
[37] C. Blackman, *ACS Sens.* **2021**, *6*, 3509.
[38] G. Jung, S. Ju, K. Choi, J. Kim, S. Hong, J. Park, W. Shin, Y. Jeong, S. Han, W. Y. Choi, J.-H. Lee, *ACS Nano* **2023**, *17*, 17790.
[39] M. Al-Hashem, S. Akbar, P. Morris, *Sens. Actuators, B* **2019**, *301*, 126845.
[40] H. Saarenpää, E. Sariola-Leikas, A. Pyymaki Perros, J. M. Kontio, A. Efimov, H. Hayashi, H. Lipsanen, H. Imahori, H. Lemmetyinen, N. V. Tkachenko, *J. Phys. Chem. C* **2012**, *116*, 2336.
[41] V. Russo, M. Ghidelli, P. Gondoni, C. S. Casari, A. L. Bassi, *J. Appl. Phys.* **2014**, *115*, 073508.
[42] R. Cuscó, E. Alarcón-Lladó, J. Ibáñez, L. Artús, J. Jiménez, B. Wang, M. J. Callahan, *Phys. Rev. B Condens. Matter. Mater. Phys.* **2007**, *75*, 165202.
[43] S. A. Studenikin, M. Cocivera, *J. Appl. Phys.* **2002**, *91*, 5060.
[44] A. Van Dijken, E. A. Meulenkamp, D. Vanmaekelbergh, A. Meijerink, *J. Lumin.* **2000**, *87*, 454.
[45] C. Baratto, E. Comini, M. Ferroni, G. Faglia, G. Sberveglieri, *CrystEngComm* **2013**, *15*, 7981.
[46] S. Lettieri, L. Santamaria Amato, P. Maddalena, E. Comini, C. Baratto, S. Todros, *Nanotechnology* **2009**, *20*, 175706.
[47] Z. M. Liao, H. Z. Zhang, Y. B. Zhou, J. Xu, J. M. Zhang, D. P. Yu, *Phys. Lett. A* **2008**, *372*, 4505.
[48] O. Casals, N. Markiewicz, C. Fabrega, I. Gràcia, C. Cane, H. S. Wasisto, A. Waag, J. D. Prades, *ACS Sens.* **2019**, *4*, 822.
[49] G. L. Long, J. D. Winefordner, **1983**, *55*.
[50] S. H. Kwon, T. H. Kim, S. M. Kim, S. Oh, K. K. Kim, *Nanoscale* **2021**, *13*, 12177.
[51] N. Ramgir, R. Bhusari, N. S. Rawat, S. J. Patil, A. K. Debnath, S. C. Gadkari, K. P. Muthe, *Mater. Sci. Semicond. Process.* **2020**, *106*, 104770.
[52] C. M. Hung, D. T. T. Le, N. Van Hieu, *J. Sci.: Adv. Mater. Devices.* **2017**, *2*, 263.
[53] V. Golovanov, V. Golovanova, T. T. Rantala, *J. Phys. Chem. Solids* **2016**, *89*, 15.
[54] V. Golovanov, V. Smyntyna, G. Mattogno, S. Kaciulis, V. Lantto, *Sens. Actuators, B* **1995**, *B26*, 108.
[55] G. Korotcenkov, V. Golovanov, V. Brinzari, A. Cornet, J. Morante, M. Ivanov, *J. Phys. Conf. Ser.* **2005**, *15*, 256.
[56] V. V. Golovanov, M. A. Mäki-Jaskari, T. T. Rantala, *IEEE Sens. J.* **2002**, *2*, 416.
[57] Z. H. Chen, Y. B. Tang, C. P. Liu, Y. H. Leung, G. D. Yuan, L. M. Chen, Y. Q. Wang, I. Bello, J. A. Zapien, W. J. Zhang, C. S. Lee, S. T. Lee, *J. Phys. Chem. C* **2009**, *113*, 13433.
[58] L. J. Brillson, Y. Lu, *J. Appl. Phys.* **2011**, *109*, 121301.
[59] K. Ip, G. Thaler, H. Yang, S. Y. Han, Y. Li, D. P. Norton, S. J. Pearton, S. Jang, F. Ren, *J. Cryst. Growth* **2006**, *287*, 149.
[60] L. J. Brillson, H. L. Mosbacker, M. J. Hetzer, Y. Strzhemechny, D. C. Look, G. Cantwell, J. Zhang, J. J. Song, *Appl. Surf. Sci.* **2008**, *254*, 8000.
[61] L. J. Brillson, H. L. Mosbacker, M. J. Hetzer, Y. Strzhemechny, G. H. Jessen, D. C. Look, G. Cantwell, J. Zhang, J. J. Song, *Appl. Phys. Lett.* **2007**, *90*, 102116.